

# Brain-Diffuser: Natural scene reconstruction from fMRI signals using generative latent diffusion

Furkan Ozcelik<sup>1,2,\*</sup> and Rufin VanRullen<sup>1,2,3</sup>

<sup>1</sup>CerCo, CNRS UMR5549, Toulouse, France

<sup>2</sup>Universite de Toulouse, Toulouse, France

<sup>3</sup>ANITI, Toulouse, France

\*ozcelikfu@gmail.com

## ABSTRACT

In neural decoding research, one of the most intriguing topics is the reconstruction of perceived natural images based on fMRI signals. Previous studies have succeeded in re-creating different aspects of the visuals, such as low-level properties (shape, texture, layout) or high-level features (category of objects, descriptive semantics of scenes) but have typically failed to reconstruct these properties together for complex scene images. Generative AI has recently made a leap forward with latent diffusion models capable of generating high-complexity images. Here, we investigate how to take advantage of this innovative technology for brain decoding. We present a two-stage scene reconstruction framework called “Brain-Diffuser”. In the first stage, starting from fMRI signals, we reconstruct images that capture low-level properties and overall layout using a VDVAE (Very Deep Variational Autoencoder) model. In the second stage, we use the image-to-image framework of a latent diffusion model (Versatile Diffusion) conditioned on predicted multimodal (text and visual) features, to generate final reconstructed images. On the publicly available Natural Scenes Dataset benchmark, our method outperforms previous models both qualitatively and quantitatively. When applied to synthetic fMRI patterns generated from individual ROI (region-of-interest) masks, our trained model creates compelling “ROI-optimal” scenes consistent with neuroscientific knowledge. Thus, the proposed methodology can have an impact on both applied (e.g. brain-computer interface) and fundamental neuroscience.

## 1 Introduction

Establishing neural encoding and decoding techniques is one way for researchers to discover how the brain and cognition work. Recent developments in modeling and computation have opened up new ways of decoding information from brain signals. Numerous studies in the field of vision research have employed statistical techniques and machine learning to decode specific information from fMRI (functional Magnetic Resonance Imaging) neural activity, such as position<sup>1</sup> or orientation<sup>2,3</sup>, to predict categories of images<sup>4,5</sup>, to match exemplar images from a candidate set<sup>6</sup>, and to reconstruct images with low levels of complexity, such as simple shapes and structures<sup>7</sup>.

In recent years, following the success in the development of deep learning models, many studies utilized deep generative models to reconstruct entire images. These deep generative models included Variational Autoencoders (VAE), Generative Adversarial Networks (GAN), and recently Latent Diffusion Models (LDM). Most of these studies used existing deep generative models, pretrained on large-scale data, and then learned a mapping (with simple regression or more advanced neural network architectures) to reconstruct the corresponding latent variables from the brain signals. This general method was used to reconstruct images with different levels of complexity such as faces<sup>8,9</sup>, single-object-centered images<sup>10</sup>, and more complex scenes<sup>11,12</sup>.

Most of the earlier works on natural scene reconstruction studied either the Generic Object Decoding<sup>13</sup> or the Deep Image Reconstruction<sup>10</sup> datasets curated by the Kamitani Lab. These datasets consist of 1200 training and 50 testing images from the ImageNet<sup>14</sup> dataset and they differ in the number of fMRI repetitions for training and testing images. One of the pioneer studies in this area is by Shen et al.<sup>10</sup> who optimized input images using a deep generator network with a loss function provided by fMRI-decoded CNN features. Beliy et al.<sup>15</sup> utilized supervised training with {fMRI, stimulus} pairs, alongside an additional consistency loss for unsupervised training with test fMRI data and additional image data. Building on this, Gaziv et al.<sup>16</sup> further improved the method by incorporating a perceptual loss on reconstructed images, resulting in sharper reconstructions. Mozafari et al.<sup>17</sup> introduced a reconstruction model based on BigBiGAN that focused on semantics. Ren et al.<sup>18</sup> devised a dual VAE-GAN model with a three-stage learning strategy that incorporates adversarial learning and knowledge distillation. Ozcelik et al.<sup>19</sup> employed the Instance-Conditioned GAN model to generate reconstructions focused on accurate semantics (by extracting semantic information with the SwAV model) and pose information (with latent optimization). Chen et al.<sup>20</sup> utilized a sparse masked brain modeling on large-scale fMRI data and then trained a double-conditioned diffusion model for visual

decoding.

Recently, Allen et al. curated another dataset for visual encoding and decoding studies called Natural Scenes Dataset<sup>11</sup>. For this dataset, 8 subjects viewed thousands of images from the COCO<sup>21</sup> dataset. COCO images contain multiple objects and they are more complex in nature compared to ImageNet images. Because of the number, diversity, and complexity of images included, the NSD dataset—although very recent—is becoming the de facto benchmark for fMRI-based natural scene reconstruction. Thus, it is the dataset that we chose for the present work. There are already three studies that reconstructed images from this dataset, and we can use them as baselines against which to compare our model’s performance. The first one is by Lin et al.<sup>12</sup>, who utilized the Lafite framework that adapts the StyleGAN2 model for text-to-image generation. The next two have not been published yet, but are publicly available as preprints. Takagi et al.<sup>22</sup> devised a method based on Stable Diffusion, using captions for the semantic information and latent variables from images for the low-level information. Gu et al.<sup>23</sup> improved upon Ozcelik et al.’s<sup>19</sup> IC-GAN framework, by establishing a surface-based convolutional network to process fMRI data instead of using vectorized data in the regression models; they also trained an encoder network to predict pose information, instead of performing latent optimization.

The above studies have fostered advances in reconstructing images with high fidelity, especially in the case of object-centered images (i.e., ImageNet images from the Kamitani dataset). Yet, reconstructing scenes with multiple objects and complex semantic descriptions (i.e., COCO images from the NSD dataset) remains a challenge. Given the remarkable recent success of latent diffusion models<sup>24</sup> in generative AI applications such as text-to-image generation<sup>24–28</sup>, we reasoned that brain decoding studies could also take advantage of such models. Thus, we propose here a visual reconstruction framework called "Brain-Diffuser", relying on the powerful generation capabilities of Versatile Diffusion<sup>28</sup>, a model conditioned on both vision and language representations acquired from the pretrained CLIP<sup>29</sup> model.

Our framework consists of two stages. The first stage, illustrated in Figure 1, generates a low-level reconstruction of images (akin to an “initial guess”) using a Very Deep Variational Autoencoder (VDVAE)<sup>30</sup>. We generate these reconstructions by training a regression model to associate fMRI signals to the corresponding latent variables of VDVAE for the same training images. In the second stage, illustrated in Figure 2, we train two additional regression models: one from fMRI patterns to CLIP-Vision features (extracted by feeding the corresponding images to the CLIP model); and the other one from fMRI patterns to CLIP-Text features (collected by providing to the CLIP model the captions of the corresponding images). Finally, we use the multimodal dual-guidance as well as the image-to-image abilities of the pretrained Versatile Diffusion (VD) model to generate the final reconstructions for test images. Using our trained regression models, for each test fMRI pattern we obtain an “initial guess” image (stage 1, VDVAE reconstruction) used by VD’s image-to-image pipeline, as well as predicted CLIP-Vision and CLIP-Text feature vectors (stage 2), jointly used for conditioning VD’s diffusion process.

We demonstrate below that the resulting scene images reconstructed by the Brain-Diffuser model are highly naturalistic and retain the overall layout and semantic information of the groundtruth images while showing only minor variations in finer details. Compared to earlier models that exhibited proficiency in capturing certain features of groundtruth images, Brain-Diffuser demonstrates qualitatively and quantitatively superior performance in terms of both high-level and low-level metrics, thus establishing itself as state-of-the-art.

## 2 Materials and Methods

### 2.1 Dataset

We used the publicly available Natural Scenes Dataset (NSD), a large-scale 7T fMRI dataset<sup>11</sup>. The NSD was collected from 8 subjects viewing images from the COCO<sup>21</sup> dataset. Each image was viewed for 3 seconds, while subjects were engaged in a continuous recognition task (reporting whether they had seen the image at any previous point in the experiment). For our study, we used the 4 subjects (sub1, sub2, sub5, sub7) who completed all trials. The training set that we used thus contained 8859 images and 24980 fMRI trials (up to 3 repetitions for each image), and 982 images and 2770 fMRI trials for the test set. We averaged fMRI trials for the images that had multiple repetitions. We also used the corresponding captions from the COCO dataset. Test images are common for all subjects, while training images are different. Generalized linear models were used to estimate preprocessed single-trial beta weights. We masked preprocessed fMRI signals using the provided NSDGeneral ROI (Region-of-Interest) mask in 1.8 mm resolution. The ROI consists of [15724, 14278, 13039, 12682] voxels for the 4 subjects respectively, and includes many visual areas from the early visual cortex to higher visual areas. For further details on this dataset and the corresponding fMRI preprocessing steps, we refer the reader to the initial paper describing the Natural Scenes Dataset<sup>11</sup>.

### 2.2 Low-Level Reconstruction of Images using VDVAE (first stage)

A Variational Auto-Encoder (VAE)<sup>31</sup> is a generative model trained to capture an input distribution (such as an image dataset) via a low-dimensional latent space, constrained to follow a particular prior distribution (e.g. Gaussian). When the input dataset

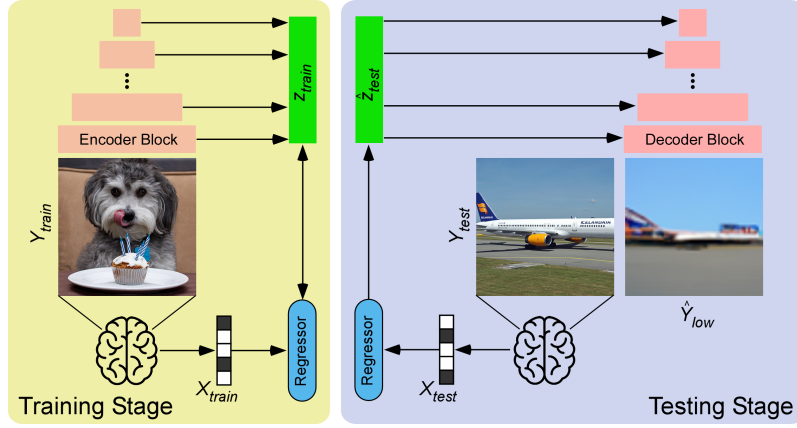


**Figure 1.** Reconstruction of Images via VDVAE (first stage). Training Stage (left). Latent variables ( $z_{train}$ ) are extracted and concatenated for the first 31 layers of the hierarchy by passing training images ( $Y_{train}$ ) into the pretrained VDVAE Encoder. A ridge regression model (Regressor) is trained between fMRI patterns ( $X_{train}$ ) and corresponding latent variables ( $z_{train}$ ). Testing Stage (right). Test fMRI data ( $X_{test}$ ) are passed through the trained Regressor to obtain predicted latent variables ( $\hat{z}_{test}$ ). These predicted latent variables are fed to the pretrained VDVAE Decoder to get the low-level reconstruction ( $\hat{Y}_{low}$ ) of the test images ( $Y_{test}$ ), which will serve as a sort of “initial guess” for the second stage. Note that all VDVAE layers (encoder and decoder blocks) are pretrained and frozen, only the brain-to-latent regression layer (blue box) is trained.

takes on a more complex distribution, training a Variational Autoencoder (VAE) can be challenging. Indeed, prior work has found that datasets consisting of natural scene images require many latent variables with complex distributions for which a simple VAE would not suffice; this is why the Very Deep Variational Autoencoder (VDVAE) was introduced<sup>30</sup>. The VDVAE is a hierarchical VAE model, with several layers of conditionally dependent latent variables, each layer adding different details from coarse to fine when transitioning from top to bottom. The hierarchical dependence can be seen in equations (1) and (2), where  $z$  indicates latent representations,  $x$  is the input variable,  $q_\phi$  represents the approximate posterior distribution that is learned when training the encoder, and  $p_\theta$  represents the prior distribution that is learned when training the decoder. The latent variable  $z_0$  is at the top of the hierarchy with the smallest dimension (low resolution, with coarse details) and  $z_N$  is at the bottom of the hierarchy with the largest dimension (high resolution, with fine details). Equation (1) shows that the latent variables at the bottom of the hierarchy are dependent on those who are at the top (and on the input  $x$ ). When there is no input ( $x$ ), it is still possible to generate samples using the prior distribution described in equation (2). This hierarchical structure helps the VDVAE learn sufficiently expressive latent variables to represent complex distributions like natural scene images.

$$q_\phi(z | x) = q_\phi(z_0 | x) q_\phi(z_1 | z_0, x) \dots q_\phi(z_N | z_{<N}, x) \quad (1)$$

$$p_\theta(z) = p_\theta(z_0) p_\theta(z_1 | z_0) \dots p_\theta(z_N | z_{<N}) \quad (2)$$

For our study, we used the model provided in<sup>30</sup>, trained on a  $64 \times 64$  resolution ImageNet dataset, and consisting of 75 layers; we only utilized the latent variables from the first 31 layers for the sake of size in regression, since we observed that adding further layers did not make much difference in the reconstruction results (at test time, the latent variables from the remaining layers are sampled according to the prior distribution given in equation (2)).

In the training stage, we fed images to the encoder part of the VDVAE to extract latent variables for each training image (as described in Figure 1). We concatenated the latent variables from the 31 layers, which resulted in 91168-dim vectors. Then, we trained a ridge regression model between fMRI training patterns and these concatenated vectors. In the testing stage, we provided test fMRI patterns to the trained regression model and thus predicted latent values for each test image. Then, we fed those latent values to the decoder part of the VDVAE and obtained reconstructed images ( $64 \times 64$  pixels) from the VDVAE. These low-level reconstructions served as an “initial guess” for the diffusion model (second stage).

### 2.3 Final Reconstruction of Images using Versatile Diffusion (second stage)

Although the VDVAE was helpful to reconstruct the layout of the image, it is not sufficient for the high-level features, nor does it produce fully naturalistic pictures. For that, we use the Versatile Diffusion<sup>28</sup> model in the second stage of our reconstruction framework. Versatile Diffusion is a recently proposed latent diffusion model (LDM)<sup>24</sup>.

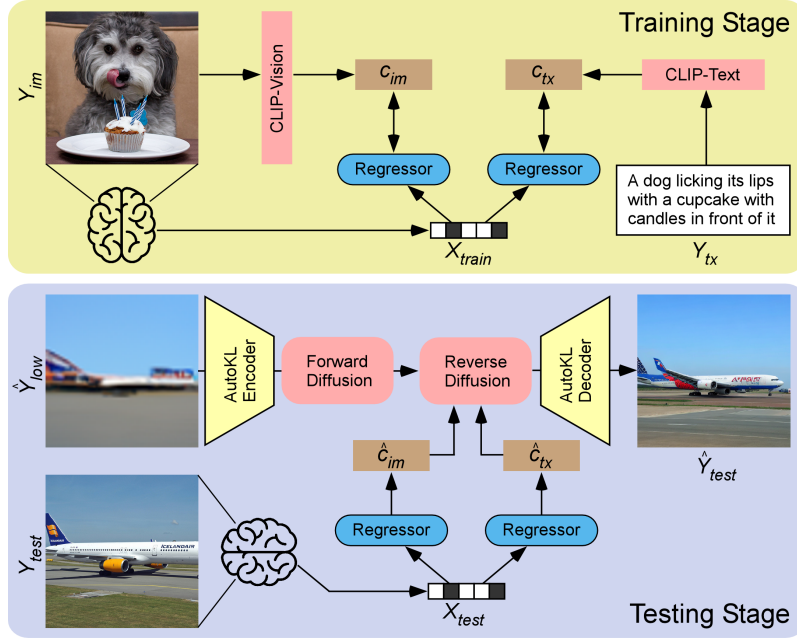


**Figure 2.** Final Reconstruction of Images via Versatile Diffusion (second stage). Training Stage: CLIP-Vision features ( $c_{im}$ ) are extracted by feeding training images ( $Y_{im}$ ) to the pretrained CLIP model. CLIP-Text features ( $c_{tx}$ ) are extracted by providing the corresponding captions ( $Y_{tx}$ ) to the pretrained CLIP Model. Two different ridge regression models (Regressors) are trained to learn the mapping between these features and fMRI patterns ( $X_{train}$ ). Testing Stage: Predicted CLIP-Vision ( $\hat{c}_{im}$ ) and CLIP-Text ( $\hat{c}_{tx}$ ) features are computed by giving test fMRI patterns ( $X_{test}$ ) to the trained regression models. In the image-to-image pipeline of the latent diffusion model, VDVAE reconstructions of test images (the “initial guess”  $\hat{Y}_{low}$  from the first stage) are passed through the AutoKL Encoder of the pretrained Versatile Diffusion model, and the obtained latent vectors undergo 37 steps of the forward diffusion process (noise addition). The resulting noisy latent vectors are used to initialize the reverse diffusion process, which is also guided by predicted CLIP-Vision ( $\hat{c}_{im}$ ) and CLIP-Text ( $\hat{c}_{tx}$ ) features jointly in a dual-guided framework. At last, the resulting denoised latent vector is passed through the AutoKL Decoder to generate the final reconstructed image ( $\hat{Y}_{test}$ ). Note that all CLIP (vision and text encoders) and Versatile Diffusion layers (AutoKL encoder and decoder, forward and reverse diffusion blocks) are pretrained and frozen, only the brain-to-latent regression layers (blue boxes) are trained.

LDMs have become highly popular after their success in high-resolution text-to-image generation. In order to train an LDM, first an autoencoder (with encoder  $E(\cdot)$  and decoder  $D(\cdot)$ ) is trained on a large-scale image dataset to learn a compressed representation of images  $x_0$ , i.e. a latent space  $z_0 = E(x_0)$ . Then, the forward diffusion process is applied to these latent variables  $z_0$  by adding Gaussian noise in successive timesteps (described in equation (3), where  $t$  represents the timestep,  $\bar{\alpha}_t$  indicates a coefficient derived from the standard deviation of the Gaussian noise, and  $\epsilon$  represents the Gaussian noise). The reverse diffusion process is learned via a neural network (Denoising U-Net in the original paper) to predict and remove noise from the noisy latent so as to retrieve the original latent variables. This is done by minimizing the loss function in equation (4), where  $\epsilon$  is the true Gaussian noise,  $\epsilon_\theta(\cdot)$  represents the neural network being trained to predict the noise,  $z_t$  is the latent variable,  $t$  is the timestep, and  $\tau_\theta(y)$  is the conditioning input for the U-Net. After the reverse diffusion process, the denoised latent variables are passed through the trained decoder  $D(\cdot)$  to generate the images. The critical part of this process is that it is possible to condition this reverse diffusion process on different representations (e.g text captions, images, semantic maps). This conditioning process is done by merging conditions ( $\tau_\theta(y)$ ) in the cross-attention block of the Denoising U-Net.

$$z_t = \sqrt{\bar{\alpha}_t} z_0 + \sqrt{1 - \bar{\alpha}_t} \epsilon \quad (3)$$

$$L_{LDM} = \mathbb{E}_{t, z_0, \epsilon, y} \left[ \|\epsilon - \epsilon_\theta(z_t, t, \tau_\theta(y))\|^2 \right] \quad (4)$$

The Versatile Diffusion model (see Figure 2) is a latent diffusion model with different pathways which allow us to condition the generation process on both text and image features to guide the reverse diffusion process. It is possible to provide



CLIP-Vision, CLIP-Text, or both features as conditions in the reverse diffusion process. It is also possible to initialize the reverse diffusion with latent variables obtained from a particular image, rather than from a purely random distribution—this is the image-to-image pipeline that we will use to take advantage of our “initial guess” image from stage 1. The Versatile Diffusion model that we utilized in our framework was trained on the Laion2B-en<sup>32</sup> dataset with  $512 \times 512$  resolution images and corresponding captions. The CLIP network used in Versatile Diffusion is based on the transformer architecture (ViT-L/14) and pretrained on a large-scale contrastive task.

In stage 2, we thus train two regression models, the first one between fMRI patterns and CLIP-Vision features (with  $257 \times 768$ -dim extracted from the corresponding images) and the second one between fMRI patterns and CLIP-Text features ( $77 \times 768$ -dim extracted from the COCO captions associated with the corresponding images). At testing time, we use the image-to-image pipeline of the latent diffusion model. First, we encode the image reconstructed with the VDVAE model (stage 1) with the AutoKL Encoder (after upsampling the image from  $64 \times 64$  to  $512 \times 512$ ) and add noise to the latent vector for 37 steps of forward diffusion (50 steps being the full diffusion). Then, we feed this noisy latent as initialization to the diffusion model and denoise it for 37 steps while conditioning with the predicted CLIP-Vision and CLIP-Text features (stage 2). In every step of reverse diffusion, we use CLIP-Vision and CLIP-Text jointly in the double-guided diffusion pipeline of Versatile Diffusion, where the cross-attention matrices for both conditions are mixed through linear interpolation (with CLIP-Vision having a relative strength of 0.6 and CLIP-Text of 0.4). The diffusion result is passed through the AutoKL Decoder to produce our final  $512 \times 512$  pixel reconstruction.

## 2.4 Code availability

The code for our project, including scripts to train regression models, pretrained weights, and scripts to produce reconstructions for test images and for ROI-based synthetic patterns, is publicly available at [github.com/ozcelikfu/brain-diffuser](https://github.com/ozcelikfu/brain-diffuser).

# 3 Results and Analyses

## 3.1 Image reconstruction examples

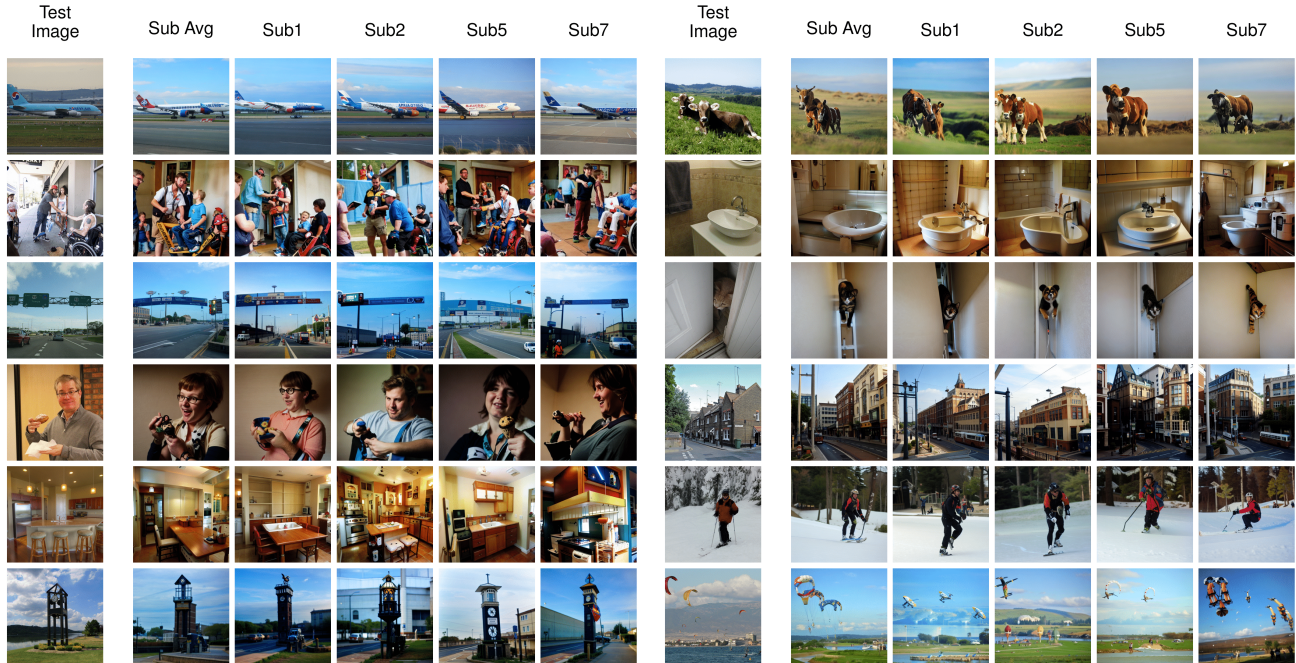


**Figure 3.** Examples of fMRI Reconstructions from our Brain-Diffuser model. The first column is the groundtruth image (Test Image). The second column is generated by averaging the predicted latent variables over all 4 subjects seeing the same picture (Sub Avg). The remaining columns are for each individual subject (Sub1, Sub2, Sub5, Sub7)

We present examples of reconstructions from our model in Figure 3. While we present the results of each individual subject in different columns, we also added results gathered by averaging the latent variables predicted by all subjects. In

general, we see that reconstructed images capture most of the layout and semantics of the groundtruth images, while there remain differences in pixel-level details. For instance, looking specifically at the first four images on the left, we see that the reconstructed pose (3D orientation) of the plane (first image) is correct for every subject although there are some differences in the details of the plane and also in the texture of the background. Nonetheless, the fact that a commercial plane on a runway, facing to the right on a blue sky background was reconstructed in all instances is not a trivial feat. For the second example, all reconstructed images display a group of people, although layouts tend to differ. Still, a person in a wheelchair is visible in the bottom right corner for three of the four subjects. For the third image, the model reconstructed a highway with road signs correctly, although the orientation of the road is different for some of the subjects, and the details of the signs are not entirely matched. On the fourth sample, all reconstructed images show a single person facing left and holding an object in their hand, as in the groundtruth image. The person’s details (gender, age, clothing) are different across subjects, e.g. with glasses only reconstructed for subject 1 and in the average across subjects. Reconstructed image contrast also differs from the ground truth. Similar conclusions can be generalized to most images of the test set: while never passing for a picture-perfect copy, the reconstructed images are always naturalistic and plausible alternate renditions of the ground truth.

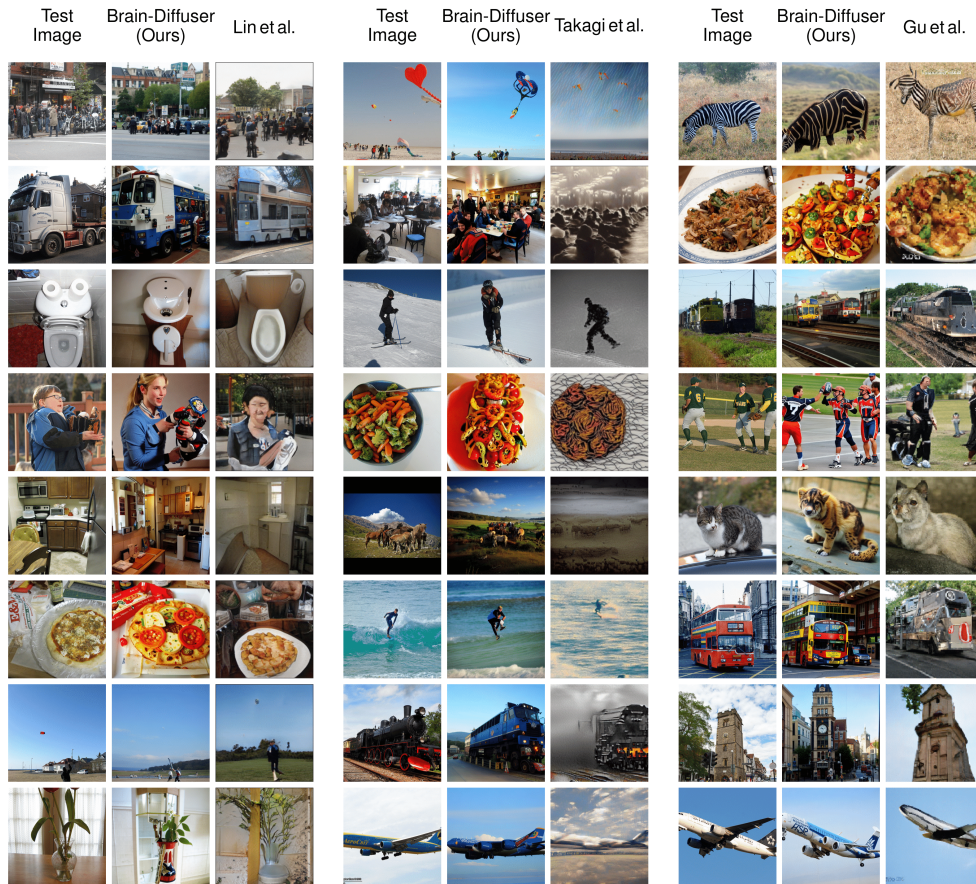


**Figure 4.** Comparison of fMRI Reconstructions for different models. Since the presented test images in all methods were different, we did comparisons separately for each model. On the left (first 3 columns), we present the comparison of our model with Lin et al. together with groundtruth test images. On the center (columns 4-6), we present the comparison of our model with Takagi et al. together with groundtruth test images. On the right (last 3 columns), we present the comparison of our model with Gu et al. together with groundtruth test images.

### 3.2 Comparison with state of the art

How do these findings compare to the state of the art? We contrast the qualitative results of our model with three other existing models in Figure 4. We selected 8 images for each model comparison; we use different images each time since these studies presented different images in their papers. (Note that for the specific purpose of comparing with Lin et al., we re-trained and re-tested our model with a different training and testing split, to match the split that they had used).



Lin et al.<sup>12</sup> was the first study that used the NSD dataset for reconstruction. They are similar to our model in terms of utilizing both image and text features as conditions, but they used a StyleGAN2 model instead of an LDM. Although Lin et al seem to be performing better than the other two prior models, in some instances the quality of their reconstructions still lags behind ours. For instance, in the second image, the details of the truck are better represented in our model. In the fourth image, the color of the clothes is presented more accurately in our model, as well as the fact that the person is holding an item; the person’s face also looks more realistic compared to Lin et al. Takagi et al.<sup>22</sup> is the only other study (in addition to ours) to use a latent diffusion model for reconstructing images from the NSD dataset. Although their model generates easily recognizable silhouettes, they do not seem to perform as well as our model in any qualitative aspect including low-level details, semantics, or naturalness. Finally, Gu et al.<sup>23</sup> used an Instance-Conditioned GAN model trained on ImageNet. When we compare our results to theirs, we can see that, although both appear good at reconstructing images with similar semantics, structural aspects are less well represented in their reconstructed images (e.g. unrealistic warped shapes for the train, bus, and building). In contrast, the shape and texture details of our model are more realistic. Also, their model trained on ImageNet seems limited in reconstructing complex scenes with multiple objects; as an example, we see one train in the third image although there are two trains in the groundtruth image, and in the reconstructed image from our model.

**Table 1.** Quantitative Analysis of fMRI Reconstructions. For each measure, the best value is in bold. (For PixCorr, SSIM, AlexNet(2), AlexNet(5), Inception and CLIP metrics, higher is better. For EffNet-B and SwAV distances, lower is better. This is indicated by the arrow pointing up or down, respectively)

Method	Quantitative Measures							
	Low-Level				High-Level			
	PixCorr ↑	SSIM ↑	AlexNet(2) ↑	AlexNet(5) ↑	Inception ↑	CLIP ↑	EffNet-B ↓	SwAV ↓
Lin et al. <sup>12</sup>	—	—	—	—	78.2%	—	—	—
Takagi et al. <sup>22</sup>	—	—	83.0%	83.0%	76.0%	77.0%	—	—
Gu et al. <sup>23</sup>	.150	.325	—	—	—	—	.862	.465
Brain-Diffuser (Ours)	<b>.254</b>	<b>.356</b>	<b>94.2%</b>	<b>96.2%</b>	<b>87.2%</b>	<b>91.5%</b>	<b>.775</b>	<b>.423</b>

### 3.3 Quantitative Results

To make the comparison with other models more quantitative, we present the results of 8 different image quality metrics in Table 1. PixCorr is the pixel-level correlation of reconstructed and groundtruth images. SSIM<sup>33</sup> is the structural similarity index metric. AlexNet(2) and AlexNet(5) are the 2-way comparisons of the second and fifth layers of AlexNet<sup>34</sup>, respectively. Inception is the 2-way comparison of the last pooling layer of InceptionV3<sup>35</sup>. CLIP is the 2-way comparison of the output layer of the CLIP-Vision<sup>29</sup> model. EffNet-B and SwAV are distance metrics gathered from EfficientNet-B1<sup>36</sup> and SwAV-ResNet50<sup>37</sup> models, respectively. The first four can be considered as low-level metrics, while the last four reflect higher-level properties. For PixCorr and SSIM metrics, we downsampled generated images from  $512 \times 512$  resolution to  $425 \times 425$  resolution (i.e the resolution of groundtruth images in NSD dataset). For the rest of the measures, generated images are preprocessed according to the input properties of each network. Note that not all measures are available for each previous model (depending on what they chose to report). However, each model has at least one point of comparison with ours. Our model is the best-performing model by a decent margin for all of the quantitative metrics. Overall, these results show that our model can be considered state-of-the-art for both low-level and high-level quantitative measures.

We also used the same 8 quality measures to evaluate various ablations of our main model, and thus determine the relative contributions of each component computed in stage 1 (Figure 1) or stage 2 (Figure 2). The results (see Supplementary Table 2 and Supplementary Figure 6) indicate that each component does provide reliable improvements to the model and that our full Brain-Diffuser model combining a low-level “initial guess” (VDVAE reconstruction, stage 1) with both CLIP-Vision and CLIP-Text guidance (stage 2) is superior to all variants.

### 3.4 ROI Analysis

Beyond brain decoding, we show here that our method can also be used to help understand the functional properties of specific regions-of-interest (ROIs) in the brain. Although we know from early studies in the neuroscience literature<sup>4,38–45</sup> what sort of visual properties would best activate neurons in each brain region, it has not been possible until now (maybe with a few exceptions<sup>19,46–48</sup>) to directly visualize an “optimal” stimulus for a given brain region. Our method can easily be adapted to address this gap. In the NSD dataset, there are different pre-existing region masks provided. The NSDGeneral mask was the one we used for training our decoding system, but there are also masks given for smaller functional and anatomical regions. We used the intersection of some of these regions with NSDGeneral, each time creating a synthetic fMRI pattern where the ROI was active (signal set to 1) and the rest of the brain inactive (signal set to 0). From this synthetic pattern, our system could



**Figure 5.** Images reconstructed from synthetic fMRI patterns created by activating specific regions-of-interests (ROIs). The first 4 rows present individual subjects: Sub1, Sub2, Sub5, and Sub7. The last row is generated by averaging the latent vectors predicted from all 4 subjects. The columns present ROIs: First four are ROIs from the visual cortex (V1-V4) gathered by population receptive field experiments, and the last four are ROIs that are specified with functional localization experiments (Face-ROI, Word-ROI, Place-ROI, Body-ROI). Histogram stretching and equalization is applied for visualization purposes.

then directly reconstruct an equivalent visual scene. We used 4 visual ROIs derived from population receptive field (pRF) experiments, and 4 ROIs derived from functional localization (fLoc) experiments. These ROIs are as follows (region names following the terminology adopted in Allen et al.<sup>11</sup>): V1 is the concatenation of V1 ventral (V1v) and V1 dorsal (V1d), and similarly for V2 and V3; V4 is the human V4 (hV4); the Face-ROI consists in the union of OFA, FFA-1, FFA-2, mTL-faces, and aTL-faces; Word-ROI consists in OWFA, VWFA-1, VWFA-2, mfs-words, and mTL-words; Place-ROI consists in OPA, PPA, and RSC; Body-ROI consists in EBA, FBA-1, FBA-2, and mTL-bodies.

In order to visualize “ROI-optimal” images, we created synthetic fMRI patterns by setting voxels of a specific ROI to ones and the rest to zeros (inspired by the analysis in Ozcelik et al.<sup>19</sup>). Then, we fed these synthetic patterns to the regression models and generated predicted latent variables. Since these fMRI patterns can be considered out-of-distribution (because there are no similar patterns in the training set), we re-normalized the generated latent variables to give them a similar euclidean norm to the training samples. This procedure helped the diffusion model to generate meaningful images that are shown in Figure 5.

Upon inspecting the generated “ROI-optimal” images for visual ROIs, we see that V1 produces high-contrast scenes with very detailed textures extending to the visual periphery, such as trees and foliage in a park with numerous small human or animal figures. V2 is similar (especially for Sub1 and Sub5, which also display humans in a luxuriant garden environment), but with slightly broader elements and less peripheral detail (e.g. trays filled with various foods in Sub2, Sub7, and in the subject-average). Continuing along the same trend, V3 and V4 produce larger objects compared to the earlier regions, with repeating patterns and global structure. V4 especially generates colorful, high-contrast objects resembling toys on a bright background.

The ROI-optimal images for functionally defined high-level ROIs are even easier to interpret, as they tend to coincide with each region’s known category preference. For instance, the model generated multiple face images for the Face-ROI, including humans and sometimes even animal faces (e.g. dogs in Sub5 and in the subject-average). For the Word-ROI, the model generated characters and pseudo-words on objects or signs (except for Sub7). Architecturally plausible indoor scene layouts were produced for the Place-ROI. Finally, for the Body-ROI, the reconstructed images show both human and animal body parts like arms and legs engaged in active behavior like sports or running. While these results mainly confirm decades of converging knowledge from the neuroscience literature on neuronal selectivity in the ventral visual pathway, it is the first time that these functional properties can be directly visualized in vivid detail and high-resolution images. Furthermore, the technique introduced here could easily be extended to study retinotopic or eccentricity-based cortical organization (see Supplementary Figure 7), to probe less well-known regions of the visual cortex, to help settle theoretical arguments about distinct sub-regions

of (e.g.) the face processing network, or to render images for arbitrary combinations of ROIs (e.g., what image would optimally activate V1, V4, and the face-ROI, but not V2 or the Body-ROI). We leave these questions open for future research.

## 4 Discussion

In this study, we designed a two-stage framework (Brain-Diffuser) that reconstructs images from fMRI patterns using generative models based on latent diffusion. In the first stage, we used the VDVAE model to generate “initial guess” reconstructions focusing on low-level details. Then in the second stage, we used the image-to-image pipeline of the Versatile Diffusion model, starting from this initial guess, to generate final reconstructions via diffusion, guided by both predicted CLIP-Vision and CLIP-Text features. As we relied on pre-trained and publicly available models for image generation (VDVAE, Versatile Diffusion) and multimodal feature extraction (CLIP), our method only required training ridge regression models from multivoxel brain activity to the relevant model latent spaces (Figures 1 and 2).

We analyzed the results both qualitatively (Figure 3) and quantitatively (Table 1). We observed that reconstructed scene images generated by Brain-Diffuser, although not perfectly identical to groundtruth images, preserve most of the layout and semantic information. They also appear more naturalistic compared to reconstructions from earlier studies (Figure 4). When evaluated quantitatively, we saw that Brain-Diffuser outperforms previous models in both high-level and low-level metrics. After advancing the state-of-the-art in image generation applications<sup>24–28</sup>, it appears that latent diffusion models can also be used to improve the state-of-the-art in fMRI-based image reconstruction.

Although latent diffusion models are very recent<sup>24</sup>, we noted at least two competing studies that used LDMs for fMRI-based image reconstruction. Neither of them has been published yet, but they are publicly available as preprints. Chen et al.<sup>20</sup> proposed MinD-Vis, a method based on an LDM conditioned on image category labels (rather than text captions) to reconstruct images from the Kamitani dataset. As mentioned above, this is a less challenging, single-object-centered dataset; thus, their results cannot be directly compared with ours, obtained using the richer and more complex NSD dataset. Takagi et al.<sup>22</sup>, on the other hand, used NSD and were thus included in our quantitative comparisons. There are multiple possible reasons why our model performed better than theirs, on both low-level and high-level metrics. Beyond the use of distinct pretrained LDMs (Stable Diffusion<sup>24</sup> for Takagi et al. vs. Versatile Diffusion<sup>28</sup> in our study), our framework contains several improvements such as the use of VDVAE reconstructions for low-level details (Figure 1) and the dual conditioning on CLIP-Vision and CLIP-Text features (Figure 2), which together resulted in better qualitative and quantitative results.

There are several ways in which this work may be pursued in the future. As deep generative models will likely continue to improve at a breakneck pace, it is probable that there will soon come models better suited for complex scene reconstruction from fMRI signals. Of course, among a pool of many generative models, it may not be a trivial task to select the most appropriate ones and to experiment on them and adapt them for brain decoding and image reconstruction. Besides improving the reconstruction quality, future work could also design novel experiments and analyses on the NSD dataset using generative models. For instance, in this study, we have shown that we can use generative models to reveal the “optimal” stimulus for anatomically, functionally or retinotopically-defined ROIs, by analyzing the reconstructions of synthetic fMRI patterns created from the corresponding ROI masks. Similar “virtual experiments” in this framework could help us address outstanding questions in neuroscience, and understand the organization of sensory and semantic knowledge in the brain.

## Acknowledgments

This work was funded by the Agence Nationale de la Recherche ANR grants AI-REPS ANR-18-CE37-0007-01 and ANITI ANR-19-PI3A-0004.

## References

1. Thirion, B. *et al.* Inverse retinotopy: inferring the visual content of images from brain activation patterns. *Neuroimage* **33**, 1104–1116 (2006).
2. Kamitani, Y. & Tong, F. Decoding the visual and subjective contents of the human brain. *Nat. neuroscience* **8**, 679–685 (2005).
3. Haynes, J.-D. & Rees, G. Predicting the orientation of invisible stimuli from activity in human primary visual cortex. *Nat. neuroscience* **8**, 686–691 (2005).
4. Haxby, J. V. *et al.* Distributed and overlapping representations of faces and objects in ventral temporal cortex. *Science* **293**, 2425–2430 (2001).
5. Cox, D. D. & Savoy, R. L. Functional magnetic resonance imaging (fmri) “brain reading”: detecting and classifying distributed patterns of fmri activity in human visual cortex. *Neuroimage* **19**, 261–270 (2003).



6. Kay, K. N., Naselaris, T., Prenger, R. J. & Gallant, J. L. Identifying natural images from human brain activity. *Nature* **452**, 352–355 (2008).
7. Miyawaki, Y. *et al.* Visual image reconstruction from human brain activity using a combination of multiscale local image decoders. *Neuron* **60**, 915–929 (2008).
8. VanRullen, R. & Reddy, L. Reconstructing faces from fmri patterns using deep generative neural networks. *Commun. biology* **2**, 1–10 (2019).
9. Dado, T. *et al.* Hyperrealistic neural decoding for reconstructing faces from fmri activations via the gan latent space. *Sci. reports* **12**, 141 (2022).
10. Shen, G., Horikawa, T., Majima, K. & Kamitani, Y. Deep image reconstruction from human brain activity. *PLoS computational biology* **15**, e1006633 (2019).
11. Allen, E. J. *et al.* A massive 7t fmri dataset to bridge cognitive neuroscience and artificial intelligence. *Nat. neuroscience* **25**, 116–126 (2022).
12. Lin, S., Sprague, T. C. & Singh, A. Mind reader: Reconstructing complex images from brain activities. In Oh, A. H., Agarwal, A., Belgrave, D. & Cho, K. (eds.) *Advances in Neural Information Processing Systems* (2022).
13. Horikawa, T. & Kamitani, Y. Generic decoding of seen and imagined objects using hierarchical visual features. *Nat. communications* **8**, 1–15 (2017).
14. Deng, J. *et al.* Imagenet: A large-scale hierarchical image database. In *2009 IEEE conference on computer vision and pattern recognition*, 248–255 (Ieee, 2009).
15. Beliy, R. *et al.* From voxels to pixels and back: Self-supervision in natural-image reconstruction from fmri. *Adv. Neural Inf. Process. Syst.* **32** (2019).
16. Gaziv, G. *et al.* Self-supervised natural image reconstruction and large-scale semantic classification from brain activity. *NeuroImage* **254**, 119121 (2022).
17. Mozafari, M., Reddy, L. & VanRullen, R. Reconstructing natural scenes from fmri patterns using bigbigan. In *2020 International joint conference on neural networks (IJCNN)*, 1–8 (IEEE, 2020).
18. Ren, Z. *et al.* Reconstructing seen image from brain activity by visually-guided cognitive representation and adversarial learning. *NeuroImage* **228**, 117602 (2021).
19. Ozcelik, F., Choksi, B., Mozafari, M., Reddy, L. & VanRullen, R. Reconstruction of perceived images from fmri patterns and semantic brain exploration using instance-conditioned gans. In *2022 International Joint Conference on Neural Networks (IJCNN)*, 1–8 (IEEE, 2022).
20. Chen, Z., Qing, J., Xiang, T., Yue, W. L. & Zhou, J. H. Seeing beyond the brain: Conditional diffusion model with sparse masked modeling for vision decoding. *arXiv preprint arXiv:2211.06956* (2022).
21. Lin, T.-Y. *et al.* Microsoft coco: Common objects in context. In *Computer Vision–ECCV 2014: 13th European Conference, Zurich, Switzerland, September 6–12, 2014, Proceedings, Part V 13*, 740–755 (Springer, 2014).
22. Takagi, Y. & Nishimoto, S. High-resolution image reconstruction with latent diffusion models from human brain activity. *bioRxiv* 2022–11 (2022).
23. Gu, Z., Jamison, K., Kuceyeski, A. & Sabuncu, M. Decoding natural image stimuli from fmri data with a surface-based convolutional network. *arXiv preprint arXiv:2212.02409* (2022).
24. Rombach, R., Blattmann, A., Lorenz, D., Esser, P. & Ommer, B. High-resolution image synthesis with latent diffusion models. In *Proceedings of the IEEE/CVF Conference on Computer Vision and Pattern Recognition*, 10684–10695 (2022).
25. Ramesh, A., Dhariwal, P., Nichol, A., Chu, C. & Chen, M. Hierarchical text-conditional image generation with clip latents. *arXiv preprint arXiv:2204.06125* (2022).
26. Nichol, A. Q. *et al.* Glide: Towards photorealistic image generation and editing with text-guided diffusion models. In *International Conference on Machine Learning*, 16784–16804 (PMLR, 2022).
27. Saharia, C. *et al.* Photorealistic text-to-image diffusion models with deep language understanding. In Oh, A. H., Agarwal, A., Belgrave, D. & Cho, K. (eds.) *Advances in Neural Information Processing Systems* (2022).
28. Xu, X., Wang, Z., Zhang, E., Wang, K. & Shi, H. Versatile diffusion: Text, images and variations all in one diffusion model. *arXiv preprint arXiv:2211.08332* (2022).

29. Radford, A. *et al.* Learning transferable visual models from natural language supervision. In *International conference on machine learning*, 8748–8763 (PMLR, 2021).
30. Child, R. Very deep {vae}s generalize autoregressive models and can outperform them on images. In *International Conference on Learning Representations* (2021).
31. Kingma, D. P. & Welling, M. Auto-encoding variational bayes. *arXiv preprint arXiv:1312.6114* (2013).
32. Schuhmann, C. *et al.* Laion-400m: Open dataset of clip-filtered 400 million image-text pairs. *arXiv preprint arXiv:2111.02114* (2021).
33. Wang, Z., Bovik, A. C., Sheikh, H. R. & Simoncelli, E. P. Image quality assessment: from error visibility to structural similarity. *IEEE transactions on image processing* **13**, 600–612 (2004).
34. Krizhevsky, A., Sutskever, I. & Hinton, G. E. Imagenet classification with deep convolutional neural networks. *Commun. ACM* **60**, 84–90 (2017).
35. Szegedy, C., Vanhoucke, V., Ioffe, S., Shlens, J. & Wojna, Z. Rethinking the inception architecture for computer vision. In *Proceedings of the IEEE conference on computer vision and pattern recognition*, 2818–2826 (2016).
36. Tan, M. & Le, Q. Efficientnet: Rethinking model scaling for convolutional neural networks. In *International conference on machine learning*, 6105–6114 (PMLR, 2019).
37. Caron, M. *et al.* Unsupervised learning of visual features by contrasting cluster assignments. *Adv. Neural Inf. Process. Syst.* **33**, 9912–9924 (2020).
38. Hubel, D. H. & Wiesel, T. N. Receptive fields, binocular interaction and functional architecture in the cat's visual cortex. *The J. physiology* **160**, 106 (1962).
39. Gross, C. G., Rocha-Miranda, C. d. & Bender, D. Visual properties of neurons in inferotemporal cortex of the macaque. *J. neurophysiology* **35**, 96–111 (1972).
40. Perrett, D., Rolls, E. & Caan, W. Visual neurones responsive to faces in the monkey temporal cortex. *Exp. brain research* **47**, 329–342 (1982).
41. Gallant, J. L., Braun, J. & Van Essen, D. C. Selectivity for polar, hyperbolic, and cartesian gratings in macaque visual cortex. *Science* **259**, 100–103 (1993).
42. Van Essen, D. C. & Gallant, J. L. Neural mechanisms of form and motion processing in the primate visual system. *Neuron* **13**, 1–10 (1994).
43. Kanwisher, N., McDermott, J. & Chun, M. M. The fusiform face area: a module in human extrastriate cortex specialized for face perception. *J. neuroscience* **17**, 4302–4311 (1997).
44. Epstein, R. & Kanwisher, N. A cortical representation of the local visual environment. *Nature* **392**, 598–601 (1998).
45. Orban, G. A., Van Essen, D. & Vanduffel, W. Comparative mapping of higher visual areas in monkeys and humans. *Trends cognitive sciences* **8**, 315–324 (2004).
46. Bashivan, P., Kar, K. & DiCarlo, J. J. Neural population control via deep image synthesis. *Science* **364**, eaav9436 (2019).
47. Gu, Z. *et al.* Neurogen: activation optimized image synthesis for discovery neuroscience. *NeuroImage* **247**, 118812 (2022).
48. Mueller, K. N., Carter, M. C., Kansupada, J. A. & Ponce, C. R. Macaques recognize features in synthetic images derived from ventral stream neurons. *Proc. Natl. Acad. Sci.* **120**, e2213034120 (2023).

## 5 Supplementary

### 5.1 Ablation studies

**Table 2.** Quantitative comparisons of test fMRI reconstructions of Sub1 with various ablations of the full model. For each measure, the best value is in bold. (For PixCorr, SSIM, AlexNet(2), AlexNet(5), Inception, and CLIP metrics, higher is better. For EffNet-B and SwAV distances, lower is better. This is indicated by the arrow pointing up or down, respectively)

Method	Quantitative Measures							
	Low-Level				High-Level			
	PixCorr $\uparrow$	SSIM $\uparrow$	AlexNet(2) $\uparrow$	AlexNet(5) $\uparrow$	Inception $\uparrow$	CLIP $\uparrow$	EffNet-B $\downarrow$	SwAV $\downarrow$
Only-VDVAE	<b>.358</b>	<b>.437</b>	<b>97.7%</b>	<b>97.6%</b>	77.0%	71.1%	.906	.581
Brain-Diffuser w/o VDVAE	.143	.302	85.6%	93.0%	87.3%	<b>92.6%</b>	.775	<b>.414</b>
Brain-Diffuser w/o CLIP-Text	.279	.333	95.6%	97.0%	<b>87.9%</b>	91.2%	.796	.436
Brain-Diffuser w/o CLIP-Vision	.327	.433	93.9%	94.1%	84.7%	84.5%	.821	.509
Brain-Diffuser	.305	.367	96.7%	97.4%	87.8%	92.5%	<b>.768</b>	.415

In order to reveal the contribution of each component of Brain-Diffuser, we performed an ablation study (with fMRI data of Sub1), and report both quantitative (Supplementary Table 2) and qualitative (Supplementary Figure 6) results.

The quantitative results are given in Supplementary Table 2. Our first ablation (Only-VDVAE) considers the results from stage-1 reconstruction only (Figure 1) without stage-2 reconstruction (Figure 2). This Only-VDVAE model provides the best results for all low-level measures, but the worst (by a large margin) for all high-level measures. This pattern of results is expected since the VDVAE reconstruction relies on low-level information without a contribution of semantic information from stage-2. By contrast, Brain-Diffuser without the VDVAE component (i.e., stage-2 reconstruction but with random initialization of the autoKL latent vector) performs worst on low-level measures (by a large margin), while it is among the best in high-level measures. This is also reasonable since this ablated model generates the reconstructions from only high-level features obtained from CLIP-Text and CLIP-Vision models and does not have much information about low-level information such as layout. Together, these results indicate that the VDVAE “initial guess” (stage-1) is necessary but not sufficient for optimal reconstruction. This is evident in the results from the full Brain-Diffuser model (last row in Supplementary Table 2), where the contribution from VDVAE (stage 1) brings strong improvements in low-level measures, with near-optimal high-level features. In another ablation, we evaluate Brain-Diffuser without CLIP-Text. Compared to the full model, there is a sizeable decrement in both low-level and high-level measures, except Inception. While the contribution of CLIP-Text to the reconstruction of high-level semantic features is expected, its improvement of low-level measures is more surprising, but could be explained by semantic information related to the image layout itself, such as the number or orientation of objects (see examples in Supplementary Figure 6). Finally, Brain-Diffuser without CLIP-Vision, surprisingly, retains high performance on the low-level PixCorr and SSIM measures (lower than Only-VDVAE, but higher than the full model); we assume that this could be due to insufficient diffusion steps (as discussed further below), preventing the reconstruction from deviating from the VDVAE initial guess. For all other measures (including low-level AlexNet measures), removing CLIP-Vision guidance severely impairs the performance of Brain-Diffuser. Overall, when jointly considering low-level and high-level measures, these quantitative results show that the full Brain-Diffuser model is better than any other variation or ablation.

We also present qualitative results in Supplementary Figure 6 with the same set of images presented in Figure 3. Reconstructions from the Only-VDVAE model (i.e., stage-1 without stage-2) match the low-level details (e.g. shapes, layouts) of the groundtruth images, but they look like vague silhouettes rather than natural images. In contrast, Brain-Diffuser without VDVAE generates images that match high-level properties (semantics) of groundtruth images but lack positional information about the objects and their layout. This is particularly clear for the fourth image in the right part of the figure, where the layout of the street and buildings is properly captured by VDVAE (and thus, also by the full model), but is lacking in the VDVAE ablation. The images generated by Brain-Diffuser without CLIP-Text appear very close to those from the full model, but with some notable differences. One example is the ski image (Row 5 on the right part of the figure), where the full model generates a single person (as in the groundtruth) while the model without CLIP-Text generates two people. Another example is the plane image (Row 1 on the left part of the figure) where the model without CLIP-Text does not produce an image with the correctly positioned plane. Finally, reconstructions from Brain-Diffuser without CLIP-Vision appear quite blurry, and somehow in-between the Only-VDVAE and the full model reconstructions. This could be an indication that forward and reverse diffusion steps were not sufficient for this model. Still, increasing the number of diffusion steps may not be a good solution since that would cause the model to lose low-level information provided by VDVAE. Overall, these qualitative examples corroborate the quantitative findings in Supplementary Table 2, and make it clear that the Brain-Diffuser model represents the optimal compromise for both low-level details and high-level semantic features.

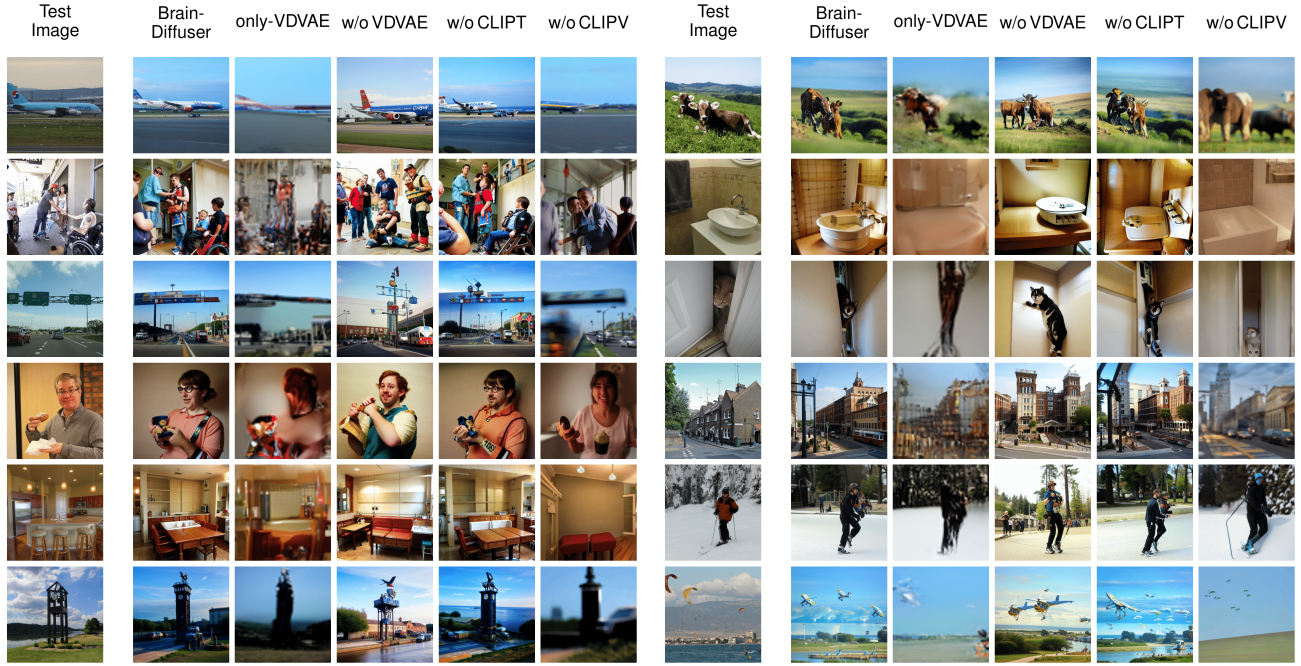


**Figure 6.** Examples of fMRI test reconstructions from Sub1 with various ablations of the full model. The first column is the groundtruth image (Test Image). The second column shows reconstructions from the full Brain-Diffuser model with all of its components. The third column is for reconstructions of the Only-VDVAE model. The remaining columns are for Brain-Diffuser with one of its components excluded, in order: without VDVAE, without CLIP-Text, and without CLIP-Vision.

## 5.2 ROI analysis for eccentricity

As a proof of concept, we also applied our ROI analysis (the same procedure reported in Figure 5) to visual regions defined by different eccentricity preferences. Similar to hierarchical regions in the visual cortex (V1, V2, V3, and hV4) these eccentricity-based regions ( $0^\circ < e < 0.5^\circ$ ,  $0.5^\circ < e < 1^\circ$ ,  $1^\circ < e < 2^\circ$ ,  $2^\circ < e < 4^\circ$  and  $4^\circ < e$ , where  $e$  stands for “eccentricity”) were also extracted by population receptive field (pRF) experiments<sup>11</sup>. These regions thus reflect the eccentricity preference of retinotopic cortex, where degrees close to  $0^\circ$  indicate central vision (closer to the fovea) and higher degrees indicate peripheral vision. The corresponding results are shown in Figure 7. It is difficult to see a clear pattern for eccentricities between  $0^\circ$  and  $0.5^\circ$  ( $0^\circ < e < 0.5^\circ$ ), as the corresponding portion of the image might be too small to be considered meaningful for the model. A noticeable aspect, however, is that all images for that ROI have detailed and high-contrast objects in the center (though there are also objects in the periphery). For eccentricities between  $0.5^\circ$  and  $1^\circ$  ( $0.5^\circ < e < 1^\circ$ ), and between  $1^\circ$  and  $2^\circ$  ( $1^\circ < e < 2^\circ$ ), we begin to see larger objects (e.g. humans, animals, blobs) at the center of the images. When we reach eccentricities between  $2^\circ$  and  $4^\circ$  ( $2^\circ < e < 4^\circ$ ) and beyond ( $4^\circ < e$ ), we start to see these objects (or animals, humans, and blobs) move towards the periphery, while the center of the images is mostly empty. These results highlight two important findings: first, the latent representations used by Brain-Diffuser (combining latent features from VDVAE, CLIP-Vision, and CLIP-Text) are precise enough to convey information about the spatial localization of objects in the image; second, we see that Brain-Diffuser managed to learn the eccentricity-based retinotopic organization of the cortex from these representations.





**Figure 7.** Images reconstructed from synthetic fMRI patterns created by activating regions-of-interest (ROIs) in the visual cortex with different eccentricities. The first 4 rows present individual subjects: Sub1, Sub2, Sub5, and Sub7. The last row is generated by averaging the latent vectors predicted from all 4 subjects. The columns present concentric regions with increasing eccentricity coverage ( $0^\circ < e < 0.5^\circ$ ,  $0.5^\circ < e < 1^\circ$ ,  $1^\circ < e < 2^\circ$ ,  $2^\circ < e < 4^\circ$ , and  $4^\circ < e$ , where “e” stands for eccentricity). Histogram stretching and equalization is applied for visualization purposes.